

The Mass Profile and Accretion History of Cold Dark Matter Halos

Aaron D. Ludlow^{1,*}, Julio F. Navarro², Michael Boylan-Kolchin³, Philip E. Bett¹, Raúl E. Angulo⁴, Ming Li^{5,6}, Simon D. M. White⁵, Carlos Frenk⁷, Volker Springel^{8,9}

¹Argelander-Institut für Astronomie, Auf dem Hügel 71, D-53121 Bonn, Germany

²Dept. of Physics and Astronomy, University of Victoria, Victoria, BC, V8P 5C2, Canada

³Center for Galaxy Evolution, 4129 Reines Hall, University of California, Irvine, CA 92697, USA

⁴Kavli Institute for Particle Astrophysics and Cosmology, Stanford University, SLAC National Laboratory, Menlo Park, CA 94025, USA

⁵Max-Planck-Institut für Astrophysik, Karl-Schwarzschild-Straße 1, 85740 Garching bei München, Germany

⁶Purple Mountain Observatory, West Beijing Rd. 2, 210008 Nanjing, China

⁷Institute for Computational Cosmology, Dept. of Physics, Univ. of Durham, South Road, Durham DH1 3LE, UK

⁸Heidelberg Institute for Theoretical Studies, Schloss-Wolfsbrunnengasse 35, 69118 Heidelberg, Germany

⁹Zentrum für Astronomie der Universität Heidelberg, ARI, Mönchhofstr. 12-14, 69120 Heidelberg, Germany

4 December 2013

ABSTRACT

We use the Millennium Simulation series to investigate the relation between the accretion history and mass profile of cold dark matter halos. We find that the mean inner density within the scale radius, r_{-2} (where the halo density profile has isothermal slope), is directly proportional to the critical density of the Universe at the time when the virial mass of the main progenitor equals the mass enclosed within r_{-2} . Scaled to these characteristic values of mass and density, the average mass accretion history, expressed in terms of the critical density of the Universe, $M(\rho_{\text{crit}}(z))$, resembles that of the enclosed density profile, $M(\langle\rho\rangle)$, at $z = 0$. Both follow closely the NFW profile, which suggests that the similarity of halo mass profiles originates from the mass-independence of halo accretion histories. Support for this interpretation is provided by outlier halos whose accretion histories deviate from the NFW shape; their mass profiles show correlated deviations from NFW and are better approximated by Einasto profiles. Fitting both $M(\langle\rho\rangle)$ and $M(\rho_{\text{crit}})$ with either NFW or Einasto profiles yield concentration and shape parameters that are correlated, confirming and extending earlier work that has linked the concentration of a halo with its accretion history. These correlations also confirm that halo structure is insensitive to initial conditions: only halos whose accretion histories differ greatly from the NFW shape show noticeable deviations from NFW in their mass profiles. As a result, the NFW profile provides acceptable fits to hot dark matter halos, which do not form hierarchically, and for fluctuation power spectra other than CDM. Our findings, however, predict a subtle but systematic dependence of mass profile shape on accretion history which, if confirmed, would provide strong support for the link between accretion history and halo structure we propose here.

Key words: cosmology: dark matter – methods: numerical

1 INTRODUCTION

Numerical simulations have shown that the equilibrium structure of cold dark matter (CDM) halos is approximately self-similar. Spherically averaged density profiles, in particular, are well approximated by scaling a simple formula pro-

posed by Navarro et al. (1995, 1996, hereafter NFW). The NFW profile has fixed shape, and is characterized by a logarithmic slope that steepens gradually from the center outwards. As such, it may be fully specified by just two parameters, usually chosen to be either the virial radius and a characteristic density or, equivalently, the halo virial mass and a concentration parameter. (See Sec. 3.1 for a summary of relevant formulae and definitions.)

* E-mail: aludlow@astro.uni-bonn.de

The gently-varying slope of the NFW profile confounded early theoretical expectations, which had envisioned a simple power-law behaviour (e.g., Fillmore & Goldreich 1984; Hoffman & Shaham 1985; Quinn et al. 1986; Crone et al. 1994), and has motivated a number of proposals to explain its origin (see, for a recent review, Frenk & White 2012). Most attempts have taken as guidance the secondary-infall model first proposed by Gunn & Gott (1972), complemented by various conjectures about the role of mergers (e.g., Salvador-Sole et al. 1998), dynamical friction (e.g., Nusser & Sheth 1999), angular momentum (e.g., Williams et al. 2004), or adiabatic invariants (e.g., Avila-Reese et al. 1998; Dalal et al. 2010), or else have argued that entropy generation during virialization might be behind the halo structural similarity (see, e.g., Taylor & Navarro 2001; Pontzen & Governato 2013).

No general consensus has yet emerged, however, reflecting the difficulty that all of these models face when trying to explain why the same NFW profile seems to fit the structure of halos formed through hierarchical clustering regardless of power spectrum (Navarro et al. 1997), as well as that of hot dark matter halos or of systems formed through monolithic collapse (e.g., Huss et al. 1999; Wang & White 2009).

In addition, none of these models provides a thorough explanation for the redshift-dependent correlations between mass and concentration seen in simulations, their scatter, or their dependence on cosmological parameters and power spectra. Halo concentration, which depends only weakly on mass, was originally linked to halo collapse time (Navarro et al. 1997), but attempts to reproduce the simulation results with simple prescriptions based on that proposal have met with limited success (Bullock et al. 2001; Eke et al. 2001; Neto et al. 2007; Macciò et al. 2008; Gao et al. 2008).

Better results have been obtained with empirical models that relate concentration to halo mass accretion history and, in particular, to the time when the main halo progenitor switches from a period of “fast growth” to one of “slow growth” (Wechsler et al. 2002; Zhao et al. 2003; Lu et al. 2006). The success of these models is not, however, unqualified. Zhao et al. (2009), for example, argue that halo concentration is determined at the time when the main progenitor first reaches 4% of the final mass, but there seems to be no natural justification for why concentration should be related to this particular, rather arbitrary time of a halo’s assembly history.

Further complicating matters, there is now convincing evidence that a number of halos have density profiles that deviate slightly, but significantly, from the NFW profile (Navarro et al. 2004). Accounting for these deviations requires the introduction of an additional *shape* parameter, thus breaking the structural similarity of CDM halos. One parameterization that results in excellent fits is the Einasto profile, where the logarithmic slope is a simple power law of radius, $d \ln \rho / d \ln r \propto (r/r_{-2})^\alpha$: the shape parameter, α , is the exponent of the power law. This finding has now been verified by additional work (Merritt et al. 2005, 2006; Navarro et al. 2010; Gao et al. 2008; Hayashi & White 2008; Stadel et al. 2009; Ludlow et al. 2011) but there is no clear understanding of what breaks the similarity or what determines the value of α for a particular halo.

We explore these issues here using a large ensemble of

halos selected from the three Millennium Simulations, MS-I (Springel et al. 2005), MS-II (Boylan-Kolchin et al. 2009), and MS-XXL (Angulo et al. 2012), collectively referred to hereafter as MS. These are amongst the largest cosmological N -body simulations available, and provide us with thousands of well-resolved halos spanning more than four decades in mass. Merger trees are available for all these simulations, making them an ideal dataset to explore the relation between accretion history and mass profiles. In addition, the numerical homogeneity and sheer size of the volumes surveyed by the MS allow us to combine large numbers of halos with similar properties to smooth out statistical fluctuations and idiosyncrasies of individual systems that might obscure the general trends. Our analysis reveals a subtle but well-defined relation between mass profile and accretion history that offers valuable new clues to the origin of the structure of CDM halos.

The plan of this paper is as follows. We describe the simulations in Sec. 2 and the analysis procedure in Sec. 3. We present our main results in Sec. 4 and summarize our main conclusions in Sec. 5.

2 NUMERICAL SIMULATIONS

Our analysis focuses on dark matter halos identified in the three Millennium Simulations. We provide here a brief summary of these simulations and of their associated halo catalogs. We refer the reader to the original papers for extensive details on each of the MS runs.

2.1 The Millennium Simulation suite

All MS runs adopt a flat, WMAP 1-normalized LCDM cosmology with the following cosmological parameters: $\Omega_m = 0.25$, $\Omega_\Lambda = 1 - \Omega_m = 0.75$, $h = 0.73$, $n = 1$ and $\sigma_8 = 0.9$. Here Ω_i is the present-day contribution of component i to the total matter energy density in units of the critical density for closure, ρ_{crit} ; σ_8 is the rms mass fluctuation in $8 h^{-1}$ Mpc spheres, linearly extrapolated to $z = 0$; n is the spectral index of primordial density fluctuations, and h is the Hubble parameter. In addition to using the same cosmological parameters, the MS runs also adopted the same sequence of outputs in order to facilitate comparisons between the runs.

MS-II follows the dark matter distribution using 2160^3 particles of mass $m_p = 6.89 \times 10^6 h^{-1} M_\odot$ in a $100 h^{-1}$ Mpc periodic box. MS-I has the same total particle number, but follows the evolution of structure in a comoving box of $500 h^{-1}$ Mpc on a side; each particle in MS-I is thus $125 \times$ more massive than in MS-II, or $m_p = 8.61 \times 10^8 h^{-1} M_\odot$. MS-XXL is the largest of the three simulations in both box size and particle number; it follows 6720^3 particles of mass $m_p = 6.17 \times 10^9 h^{-1} M_\odot$ in a $3 h^{-1}$ Gpc box.

2.2 Halo Catalogs

A friends-of-friends (FOF) group finder (Davis et al. 1985) was run on the fly for each simulation output using a linking length of $b = 0.2$ times the mean inter-particle separation and a minimum particle number $N_{\text{min}} = 20$. The subhalo

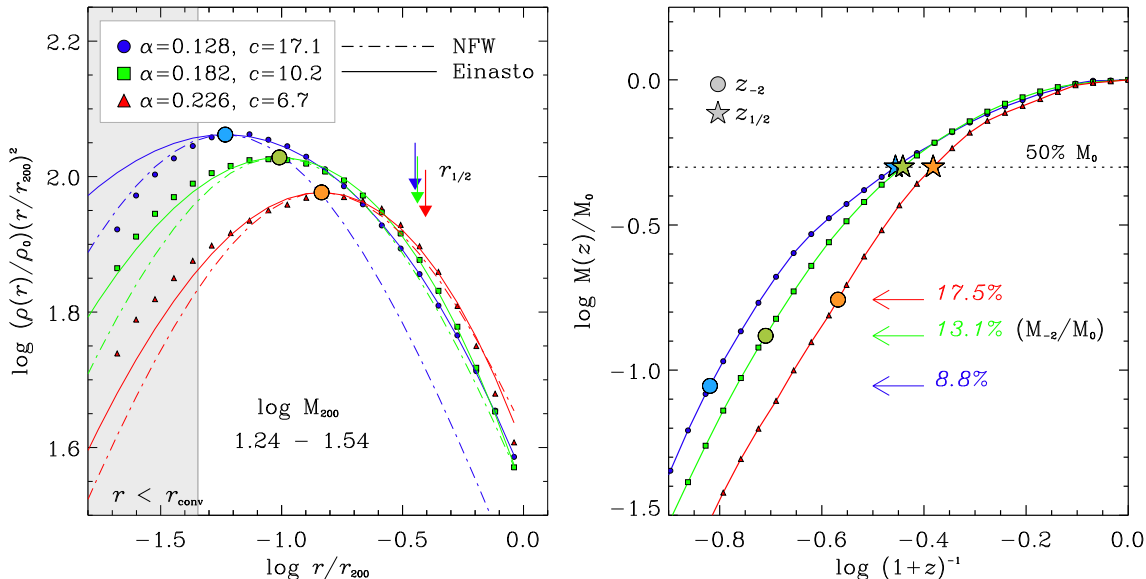


Figure 1. Halo density profiles and accretion histories. *Left panel:* Median density profiles of MS-II relaxed halos in the mass range $1.24 < \log M_{200}/(10^{10} h^{-1} M_{\odot}) < 1.54$ (corresponding to particle numbers in the range $2.5 \times 10^4 < N_{200} < 5 \times 10^4$), selected according to their concentration (see boxes in the top panel of Fig. 2). Densities are shown scaled to ρ_0 , the critical density at $z = 0$, and weighted by r^2 in order to enhance the dynamic range of the plot. Radii are scaled to the virial radius, r_{200} . The best-fit Einasto profiles are shown by the thin solid curves, with parameters listed in the legend. Dot-dashed curves indicate NFW profiles (whose shape is fixed in these units) matched at the scale radius, r_{-2} , where the $r^2\rho$ profiles peak. Arrows indicate the half-mass radius, $r_{1/2}$. *Right panel:* Median mass accretion histories (MAH) of the same set of halos chosen for the left panel. Halo accretion history is defined as the evolution of the mass of the main progenitor, expressed in units of the mass of the halo at $z = 0$. The heavy circles indicate the redshift, z_{-2} , when the progenitor’s mass equals the mass, M_{-2} , enclosed within the scale radius at $z = 0$. Starred symbols indicate the half-mass formation redshift.

finder SUBFIND, (Springel et al. 2001) was then run to identify self-bound substructure within each FOF halo.

SUBFIND dissects each FOF halo into one dominant structure (the main halo) and a number of subhalos that trace the self-bound remnants of accreted systems. We will focus our analysis on main halos identified at $z = 0$ that contain at least $N_{200} = 5000$ particles within their virial radius¹

Since dark matter halos are dynamical systems, transients induced by mergers or ongoing accretion can lead to rapid fluctuations in the structure of a halo that are poorly captured with simple fitting formulae. We therefore impose three criteria to flag systems that are clearly out of equilibrium. We consider a halo to be dynamically “relaxed” if it simultaneously satisfies all three of the following conditions (Neto et al. 2007): (i) $f_{\text{sub}} < 0.1$, (ii) $d_{\text{off}} < 0.07$ and (iii) $2T/|U| < 1.35$. Here f_{sub} is the fraction of the halo’s virial mass contributed by subhalos, $d_{\text{off}} = |\mathbf{r}_p - \mathbf{r}_{\text{CM}}|/r_{200}$ is the distance between the halo barycenter and the location of its potential minimum, expressed in units of r_{200} ; and $2T/|U|$ is the virial ratio of kinetic to potential energies, measured in the halo rest frame. None of our conclusions are heavily affected by these restrictions. Unrelaxed systems make up only

20% of all halos with virial mass of order $10^{12} M_{\odot}$ and 25% of $\sim 10^{13} M_{\odot}$ halos. Only at very large halo masses, such as cluster-sized $\sim 10^{14} M_{\odot}$ systems, the unrelaxed fraction exceeds 50%. We refer the reader to Neto et al. (2007) for further discussion of these criteria, and to Ludlow et al. (2012) for a discussion of how the inclusion of out-of-equilibrium systems may impact the mass-concentration relation at large halo masses.

3 ANALYSIS

3.1 Fitting Formulae

We consider two different formulae to fit halo density profiles. The NFW profile is given by

$$\frac{\rho(r)}{\rho_{\text{crit}}} = \frac{\delta_c}{(r/r_s)(1+r/r_s)^2}, \quad (1)$$

where r_s is a scale radius, $\rho_{\text{crit}} \equiv 3H^2/8\pi G$ is the critical density, and δ_c is the halo dimensionless characteristic density. These two parameters can also be expressed in terms of the halo virial mass, M_{200} , and a concentration parameter, $c = r_{200}/r_s$, which is related to δ_c by

$$\delta_c = \frac{200}{3} \frac{c^3}{[\ln(1+c) - c/(1+c)]}. \quad (2)$$

Note that for given mass the NFW profile has a single free parameter, the concentration. This profile can also be expressed in terms of the enclosed mean density, $M(\langle\rho\rangle)$, where

¹ We define the virial radius, r_{200} , of a halo as the radius of a sphere centered at the potential minimum that encloses a mean density of $200 \times \rho_{\text{crit}}$. We identify all virial quantities (i.e., measured within r_{200}) with a “200” subscript. Note that all particles are used to compute r_{200} , not just those bound to the main halo.

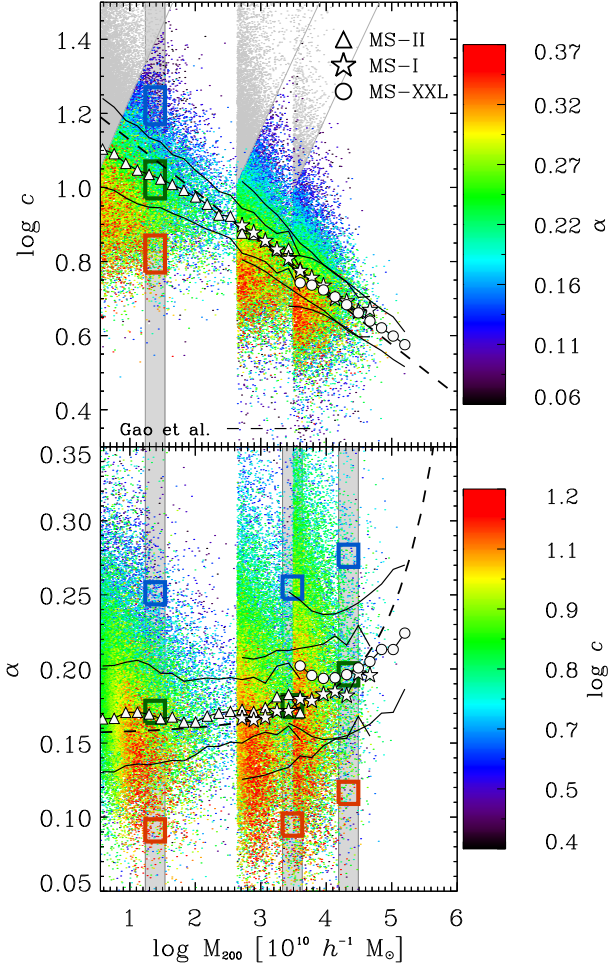


Figure 2. Mass dependence of the best-fit Einasto parameters for all halos in our sample at $z = 0$. Only relaxed halos with more than 5000 particles within the virial radius are considered. The top and bottom panels show, respectively, the concentration, $c = r_{200}/r_{-2}$, and shape parameter, α , as a function of halo virial mass. Individual points are colored according to the third parameter (see color bar on the right of each panel). Connected symbols trace the median values for each Millennium Simulation (see legend in the top panel); thin solid lines delineate the 25 to 75 percentile range. The dashed curves indicate the fitting formulae proposed by Gao et al. (2008). For clarity only 10,000 halos per simulation are shown in this figure. Halos shown in grey are systems where the best-fit scale radius is smaller than the convergence radius; these fits are deemed unreliable and the corresponding halos are not included in the analysis. Grey vertical bars highlight three different mass bins used to explore parameter variations at fixed halo mass (see Sec. 4.3 and 4.4). Small boxes indicate halos in each of those bins with average, higher-than-average, and lower-than-average values of α (bottom panel) or of the concentration (top panel).

$$\langle \rho \rangle(r) = \frac{M(< r)}{(4\pi/3)r^3} = \frac{200}{x^3} \frac{Y(cx)}{Y(c)} \rho_{\text{crit}}, \quad (3)$$

where $x = r/r_{200}$ and $Y(u) = \ln(1+u) - u/(1+u)$.

The Einasto profile (Einasto 1965) has an extra free parameter, the shape parameter α , and may be written as

$$\ln\left(\frac{\rho_E}{\rho_{-2}}\right) = -\frac{2}{\alpha} \left[\left(\frac{r}{r_{-2}}\right)^\alpha - 1 \right]. \quad (4)$$

The parameter r_{-2} marks the radius where the logarithmic slope of the density profile is equal to -2 . The same property holds for the NFW scale radius, r_s , and therefore, for short, we shall hereafter refer to the scale radius of either profile as r_{-2} . Quantities measured at (or within) r_{-2} will be denoted by a “ -2 ” subscript; e.g., $\langle \rho_{-2} \rangle = \langle \rho \rangle(r_{-2})$. Of course, like NFW, the Einasto profile may also be expressed in terms of its enclosed mean density profile, $M(\langle \rho_E \rangle)$.

We note that, for given concentration, an Einasto profile with $\alpha \approx 0.18$ resembles closely an NFW profile over roughly two decades in radius or enclosed mass. Profiles with other values of α deviate systematically from the NFW shape (see, e.g., Navarro et al. 2004, 2010).

3.2 Profile Fitting

Our analysis deals primarily with the spherically averaged density profiles of relaxed CDM halos identified at $z = 0$ in each MS. We construct radial profiles using 32 concentric bins, equally spaced in $\log r$, spanning the radial range $-2.5 \leq \log r/r_{200} \leq 0$.

The Einasto profile has three free parameters: ρ_{-2} , r_{-2} , and α . These are simultaneously adjusted in order to minimize its rms deviation from the binned density profiles. In practice, we define a figure of merit,

$$\psi^2 = \frac{1}{N_{\text{bin}}} \sum_{i=1}^{N_{\text{bin}}} [\ln \rho_i - \ln \rho_E(\rho_{-2}; r_{-2}; \alpha)]^2, \quad (5)$$

which is minimized to obtain the best-fitting set of parameters for any given halo. Equation 5 weights equally all logarithmic radial bins and, for a given radial range, is approximately independent of the number of bins used. It measures deviations of the true profile from the model caused by systematic shape differences as well as by transient features induced by, for example, substructures or tidal streams. These features lead to highly correlated bin-to-bin deviations that typically dominate over the Poisson noise in the individual radial bins. For this reason we have decided to weight all bins equally (see Navarro et al. 2010, for further discussion).

In practice, the parameters ρ_{-2} and r_{-2} can be expressed in a variety of equivalent forms, such as virial mass and concentration (M_{200}, c), or the magnitude and location of the peak in the circular velocity curve ($V_{\text{max}}, r_{\text{max}}$). In order to ease comparisons with previous work, we characterize the dark matter halo mass profile in terms of its virial mass $M_0 = M_{200}(z = 0)$, its concentration $c = r_{200}/r_{-2}$, and its Einasto “shape” parameter, α . The Einasto profile provides an excellent description of the density profile of relaxed MS halos: the median value of ψ is just $0.073_{-0.011}^{+0.014}$, where the range represents the 25th and 75th percentiles.

An analogous procedure is used when NFW fits need to be performed; in this case, the two parameters estimated by

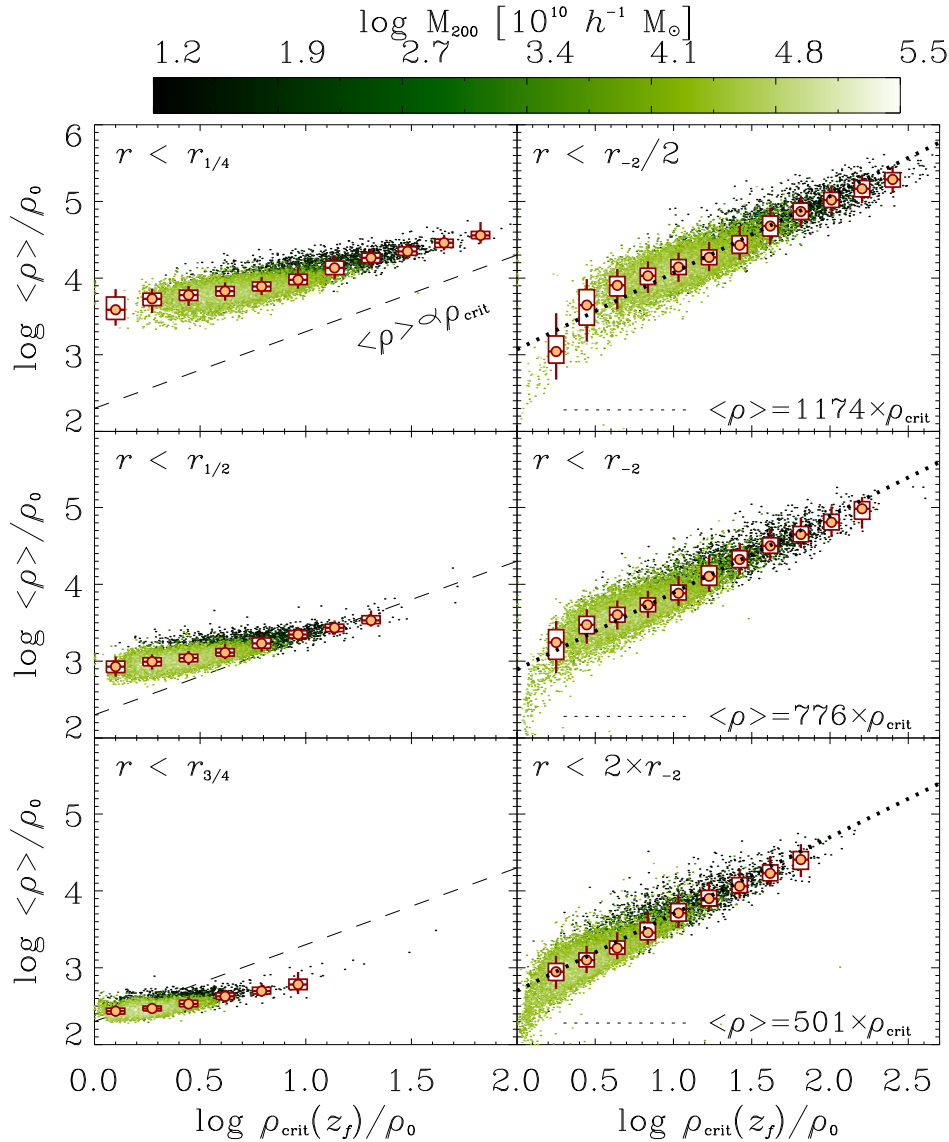


Figure 3. Relation between mass profiles at $z = 0$ and accretion histories for relaxed, well-resolved halos ($N_{200} > 2.5 \times 10^4$) in our sample. Individual halos are colored by mass, according to the color bar at the top of the plot. *Left panels:* Mean enclosed densities within the radii, $r_{1/4}$, $r_{1/2}$, and $r_{3/4}$, containing, respectively, 25%, 50% and 75% of the virial mass, shown as a function of the (critical) density of the Universe at the time when the progenitor’s virial mass equals the mass enclosed within each of those radii at $z = 0$. These densities are correlated, as expected if denser halos collapse earlier. However, the dependence varies with radius and is generally quite weak. This explains, for example, why measures of halo density (such as the concentration) correlate only poorly with the half-mass formation time. Medians, quartiles, and 10/90 percentiles are indicated by the box-and-whisker symbols. *Right panels:* As the left panels, but for radii equal to half, one, and two times the scale radius, r_{-2} . The dotted line indicates direct proportionality, scaled vertically to best fit the data of each panel (fit parameters given in the legends). The excellent agreement between this simple scaling and the data implies that, expressed in units of the scale radius, the shape of the mass profile of a halo is intimately related to that of the accretion history of its main progenitor.

the fit can also be expressed as the virial mass and concentration.

The fits are carried out over a radial range $r_{\min} < r < r_{200}$. The fitting procedure yields robust estimates for ρ_{-2} , r_{-2} and α , provided r_{\min} is chosen to be the minimum of either r_{conv} or $0.05 \times r_{200}$. Here, r_{conv} is the convergence radius defined by Power et al. (2003), where circular velocity profiles converge to better than $\sim 10\%$.

3.3 Mass Profiles and Accretion Histories

The left panel of Fig. 1 illustrates the role of c and α in describing the density profile. This figure shows the density profile of MS-II halos selected in a narrow range of mass, $1.24 < \log M_{200}/10^{10} h^{-1} M_{\odot} < 1.54$. (Densities are weighted by r^2 in order to enhance the dynamic range of the plot.) Each profile corresponds to different systems, grouped

by concentration: green squares track the median² profile of halos with average concentration for that mass; blue circles and red triangles correspond to halos with concentration $\sim 50\%$ higher and lower than the average, respectively (see boxes in the top panel of Fig. 2).

In the scaled units of Fig. 1 the scale radius, r_{-2} , signals the location of the maximum of each curve, and different concentrations show as shifts in the position of the maxima, which are indicated by large filled circles. In addition to their different concentrations, the profiles differ as well in α , which increases with decreasing concentration (see legends in Fig. 1). Arrows indicate the half-mass radius of each profile. Dot-dashed curves show NFW profiles (whose shape is fixed in this plot) with the same concentration as the best Einasto fit (solid lines). The density profile curves more gently than NFW for $\alpha \lesssim 0.18$ and less gradually than NFW for $\alpha \gtrsim 0.18$, respectively.

The (median) mass accretion histories corresponding to the same sets of halos are shown in the right-hand panel of Fig. 1. We define the mass accretion history (MAH) of a halo as the evolution of the virial mass of the main progenitor³, usually expressed as a function of the scale factor $a = 1/(1+z)$, and normalized to the present-day value, $M_0 = M_{200}(z=0)$. As expected, more concentrated halos accrete a larger fraction of their final mass earlier on. Filled stars indicate the “half-mass formation redshift”, $z_{1/2}$, whereas filled circles indicate z_{-2} , the redshift when the mass of the main progenitor first reaches M_{-2} , the mass enclosed within r_{-2} at $z=0$.

4 RESULTS

4.1 The mass-concentration-shape relations

The top panel of Fig. 2 shows the mass-concentration relation for our sample of relaxed halos at $z=0$. Concentrations are estimated from Einasto fits, and are color coded by the shape parameter, α , as indicated by the color bar. Open symbols track the median concentrations as a function of mass. Thin solid lines trace the 25th and 75th percentiles of the scatter at fixed mass. Different symbols are used for the different MS runs, as specified in the legend. Note the excellent agreement in the overlapping mass range of each simulation, which indicates that our fitting procedure is robust to the effects of numerical resolution.

The bottom panel of Fig. 2 shows the mass- α relation, colored this time by concentration. The trend is again consistent with earlier work; the median values of α are fairly insensitive to halo mass, except at the highest masses, where it increases slightly. The mass-concentration-shape trends are consistent with earlier work; for example, the dashed lines correspond to the fitting formulae proposed by Gao et al. (2008) and reproduce the overall trends very well.

Fig. 2 illustrates an interesting point already hinted at in Figure 1: the shape parameter seems to correlate with

concentration at given mass. Interestingly, *halos of average concentration have approximately the same shape parameter* ($\alpha \approx 0.18$, i.e., quite similar to NFW), regardless of mass. Halos with higher-than-average concentration have smaller values of α and vice versa. This suggests that the same mechanism responsible, at given mass, for deviations in concentration from the mean might also be behind the different mass profile shapes at $z=0$ parameterized by α . We explore this possibility next.

4.2 Characteristic densities and assembly times

As pointed out by Navarro et al. (1997) and confirmed by subsequent work (see, e.g., Jing 2000), the scatter in concentration is closely related to the accretion history of a halo: the earlier (later) a halo is assembled the higher (lower) its concentration.

This is clear from the assembly histories shown in Fig. 1, which illustrate as well that defining “formation time” in a way that correlates strongly and unequivocally with concentration is not straightforward. For example, the often-used half-mass formation redshift, $z_{1/2}$, varies only weakly with c , making it an unreliable proxy for concentration (Neto et al. 2007). *An ideal definition of formation time would result in a natural correspondence between the characteristic density of a halo at $z=0$ and the density of the Universe at the time of its assembly.*

We explore two possibilities in Fig 3. Here we show the mean density enclosed within various characteristic radii at $z=0$ versus the critical density of the Universe at the time when the main progenitor mass equals the mass enclosed within the same radii.

The left panels correspond to radii enclosing 1/4, 1/2, and 3/4 of the virial mass of the halo. Dots indicate individual halos colored by halo mass, as shown in the color bar at the top. Boxes and whiskers trace the 10th, 25th, 75th, and 90th percentiles in bins of ρ_{crit} . Note the tight but rather weak (and non-linear) correlation between densities at these radii. This confirms our earlier statement that “half-mass” formation times are unreliable indicators of halo characteristic density: halos with very different $z_{1/2}$ may nevertheless have similar concentrations.

The right-hand panels of Fig. 3 show the same density correlations, but measured at various multiples of r_{-2} , the scale radius of the mass profile at $z=0$. The middle panel shows that the mean density within r_{-2} , $\langle \rho_{-2} \rangle = M_{-2}/(4\pi/3)r_{-2}^3$, is *directly proportional* to the critical density of the Universe at the time when the virial mass of the main progenitor equals M_{-2} . Intriguingly, this is also true at $r_{-2}/2$ (top right panel) and at $2 \times r_{-2}$ (bottom right panel), although with different proportionality constants (listed in the figure legends).

This means that there is an intimate relation between the mass profile of a halo and the shape of its mass accretion history, in the sense that, once the scale radius is specified, the MAH can be reconstructed from the mass profile, and vice versa. Since mass profiles are nearly self-similar when scaled to r_{-2} , this implies that accretion histories must also be approximately self-similar when scaled appropriately. The MAH self-similarity has been previously discussed by van den Bosch (2002), but its relation to the

² Median profiles are computed at each radius after scaling all individual profiles as in Fig. 1.

³ The main progenitor of a given dark matter halo is found by tracing backwards in time the most massive halo along the main branch of its merger tree.

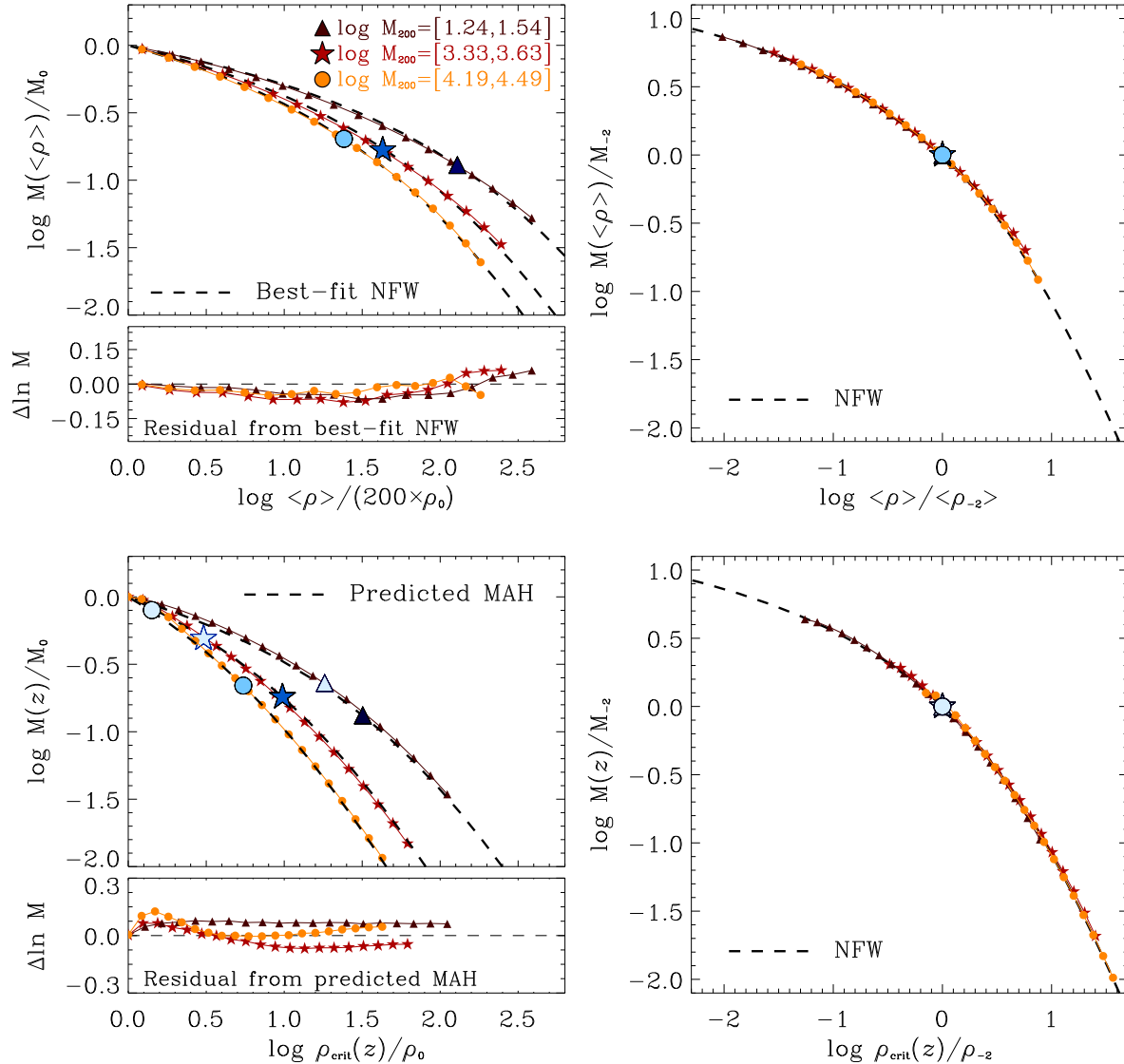


Figure 4. Average mass profiles at $z = 0$ and accretion histories for halos in three different mass bins (see shaded regions in the bottom panel of Fig. 2). *Top left:* Average mass profiles of all halos in each bin, plotted as enclosed mass (in units of M_{200}), versus inner density (in units of $200 \times$ the critical density). Dashed lines are best-fit NFW profiles, which have a single adjustable parameter, the concentration, $c = r_{200}/r_{-2}$. Heavy filled symbols indicate the enclosed mass, M_{-2} , and density, $\langle \rho_{-2} \rangle$, at the scale radius of each profile. Residuals from the best fits are shown in the bottom inset. *Top right:* Same as top-left panel, but scaled to the enclosed mass, M_{-2} , and overdensity, $\langle \rho_{-2} \rangle$, at the scale radius. Scaled in this manner, halo mass profiles all look alike and are very well approximated by an NFW profile (dashed curve). *Bottom left:* Average accretion histories of the same halos shown in the top panels. The plots show the growth of the virial mass of the main progenitor, normalized to the final mass at $z = 0$, as a function of time, expressed in terms of the critical density of the Universe at each redshift. The dashed curves are *not* fits to the data. Rather, they indicate accretion histories parameterized, as in the top panel, by an NFW profile in this M - ρ plane. The single adjustable parameter to these profiles is fully specified by the filled heavy symbols, which indicate M_{-2} , chosen to match that of the mass profiles (top-left panel) and by $\rho_{\text{crit}}(z_{-2})$, computed as $776 \langle \rho_{-2} \rangle$ following the correlation shown in the middle panel of Fig. 3. The light-colored heavy symbols indicate the scale mass and density of the predicted NFW profile; dark filled symbols mark the location of the halo characteristic mass and the corresponding formation time. *Bottom right:* Same accretion histories as in the bottom-left panel, but scaled to the characteristic values of the MAH: M_{-2} and $\langle \rho_{-2} \rangle$ (light heavy symbols in the bottom-left panel). Note the remarkable similarity in the shape of the halo mass profiles at $z = 0$ and that of the accretion histories of their main progenitors.

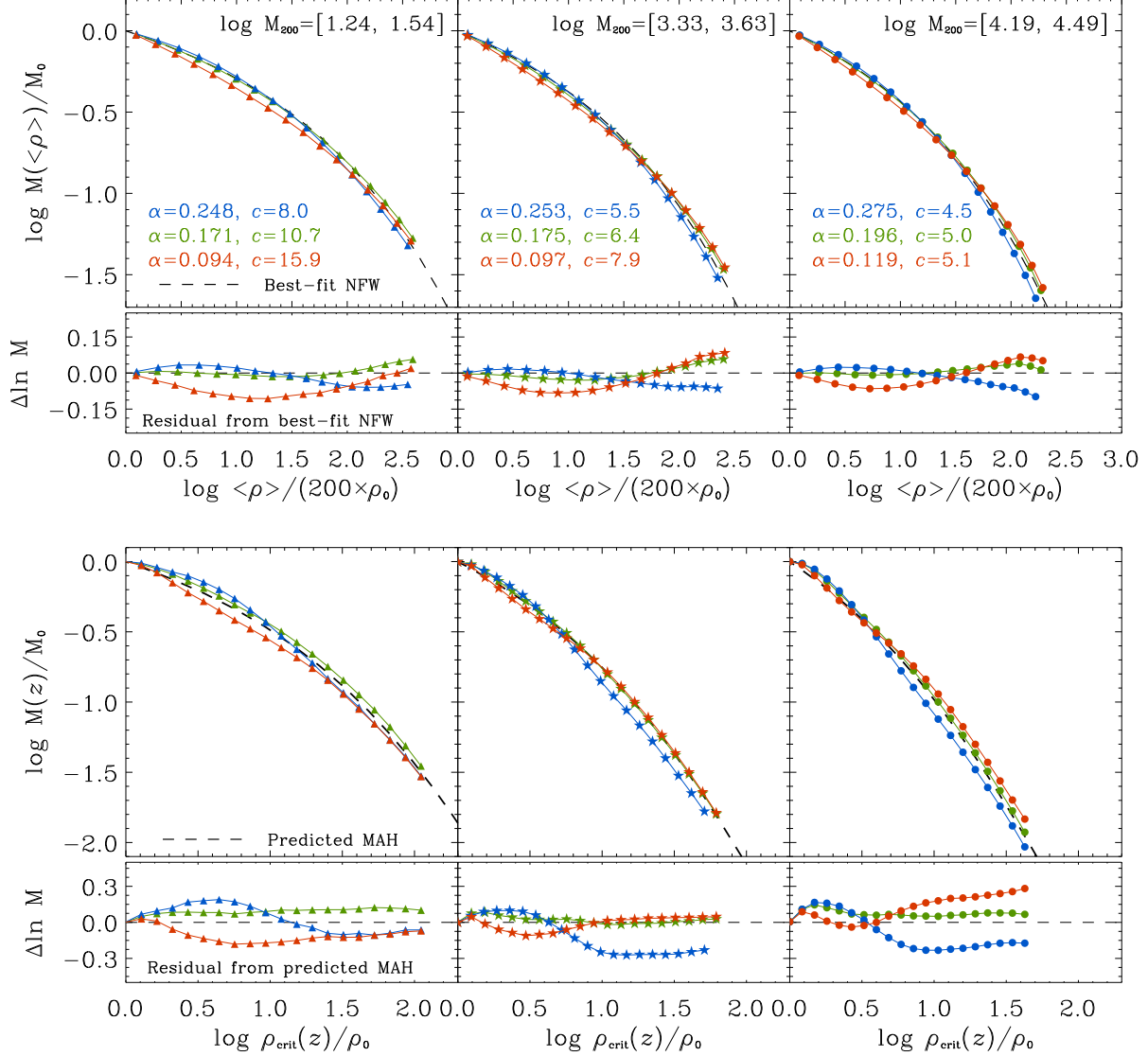


Figure 7. As Fig. 4 but for halos with higher-than-average (blue), average (green), or lower-than-average (red) values of the Einasto parameter α (see boxes in the bottom panel of Fig. 2). Left, middle, and right panels correspond to each of the three mass bins, as indicated in the legends. *Top panels:* Average mass profiles compared with the best-fit NFW profile for all halos of the same mass (see top left panel of Fig. 4). Residuals from that profile are shown at the bottom of each panel. Note the similarity between the residual curves of similar color at all masses. Different values of α imply different profile shapes, and deviate systematically from NFW. *Bottom panels:* Average mass accretion histories corresponding to the same halos as in the top panels. The dashed curves indicate the average “NFW accretion histories” for each mass bin, as shown in the bottom-left panel of Fig. 4. Residuals from this average history are shown in the bottom inset of each panel. Note the similarity between the shape of the residual curves of similar colors in all panels. This indicates that the mass accretion history is intimately linked to the mass profile at $z = 0$. Halos that, at $z = 0$, have mass profiles that deviate from NFW in a particular way have accretion histories that deviate from the NFW shape in a similar way.

shape of the mass profile, as highlighted here, has so far not been recognized.

4.3 NFW accretion histories and mass profiles

We explore further the relation between MAH and mass profile by casting both in a way that simplifies their comparison, i.e., in terms of mass versus density. In the case of the mass

profile, this is just the enclosed mass-mean inner density relation, $M(<\rho>)$ (see Sec. 3.1). For the MAH, this reduces to expressing the virial mass of the main progenitor in terms of the critical density, rather than the redshift, $M(\rho_{\text{crit}}(z))$. In what follows, we shall scale all masses to the virial mass of the halo at $z = 0$, M_0 ; $\rho_{\text{crit}}(z)$ to the value at present, ρ_0 ; and $\langle\rho\rangle$ to $200\rho_0$.

The top-left panel of Fig. 4 shows, in these scaled units,

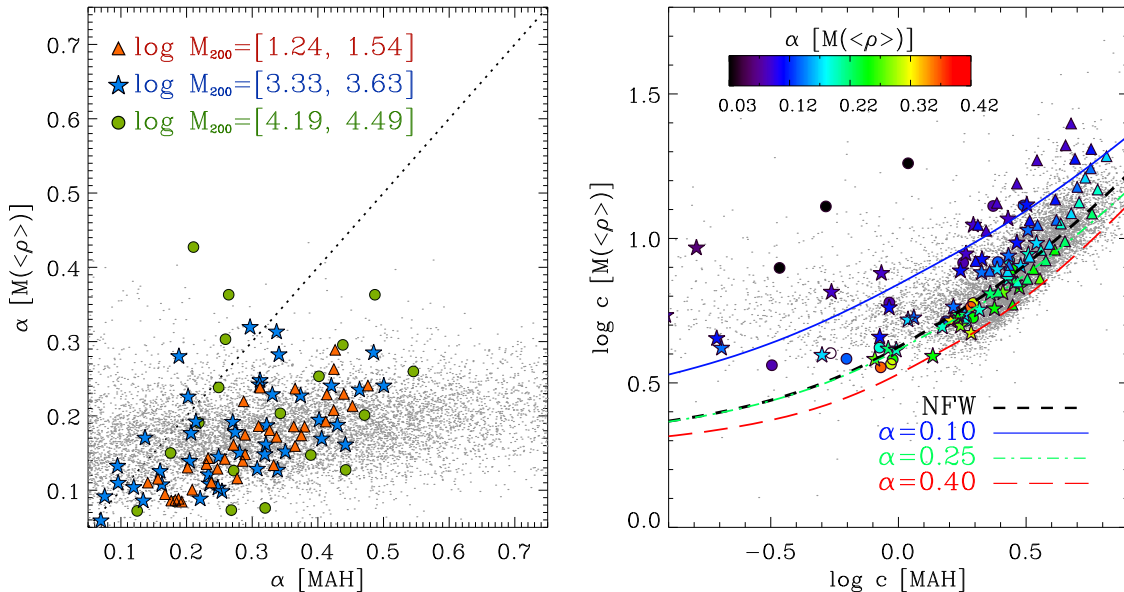


Figure 8. Concentrations and shape parameters of Einasto profiles fitted to either accretion histories or mass profiles at $z = 0$. Heavy symbols correspond to well-resolved halos grouped according to the c and α parameters of their mass profile (see details in the text). Grey dots correspond to individual halos in the same three mass bins chosen in Fig. 7. The left panel shows that the shape of the mass accretion history and that of the mass profile are correlated. The panel on the right is analogous to Fig. 5 and shows that the same applies to the concentrations. In this case, the relation depends on the value of α , as shown by the colored lines labelled in the legend. The heavy symbols are of the same type as in the left panel, but colored by α (see inset). Note that the correlations are relatively shallow, implying that even large departures from NFW-like mass accretion histories lead only to minor deviations from NFW in the mass profiles.

the average $M(\langle\rho\rangle)$ profile for halos in three different narrow mass bins (indicated by grey vertical bars in the bottom panel of Fig. 2). These mean profiles are computed by averaging halo masses, for given $\langle\rho\rangle$, after scaling all individual halos as indicated above. As expected, each profile is well fit by an NFW profile where the concentration increases gradually with decreasing mass. The heavy symbols on each profile indicate the value of M_{-2} and $\langle\rho_{-2}\rangle$. The top-right panel shows the same data, but scaled to these characteristic masses and densities. Clearly the three profiles follow closely the same NFW shape, which is fixed in these units.

The corresponding MAHs, computed as above by averaging accretion histories of scaled individual halos, are shown in the bottom-left panel of Fig. 4. The heavy symbols on each profile again indicate the value of M_{-2} (as in the above panel), as well as $\rho_{\text{crit}}(z_{-2}) = 776 \langle\rho_{-2}\rangle$, computed using the relation shown in the middle-right panel of Fig. 3.

In these scaled units, a single point can be used to specify the “concentration” of an NFW profile, which is shown by the dashed curves. Interestingly, these provide excellent descriptions of the MAHs: rescaled to their own characteristic density and mass they all look alike and also follow closely the NFW shape (bottom-right panel of Fig. 4). *The mass accretion histories and mass profiles of CDM halos are not only nearly self-similar: they both have similar shapes that may be approximated very well by the NFW profile.*

This implies that the concentration of the mass profile just reflects the “concentration” of the MAH. Indeed, assuming that the NFW shape holds for both, the relation $\rho_{\text{crit}}(z_{-2}) = 776 \langle\rho_{-2}\rangle$ delineates a unique relation between the two concentrations, which is shown as a dashed line in

Table 1. Parameters obtained for best-fits of eq. 6 to the concentration-concentration relations for NFW profiles and for Einasto profiles with several values of the shape parameter α . For all cases provided, fits are accurate to better than $\lesssim 3\%$ over the range $-0.5 \leq \log c [\text{MAH}] \leq 1.5$

NFW			
	a_1	a_2	a_3
	2.521	0.729	0.988
Einasto			
α	a_1	a_2	a_3
0.10	4.124	0.849	0.833
0.15	3.365	0.692	0.899
0.20	2.946	0.614	0.953
0.25	2.697	0.557	1.003
0.30	2.504	0.530	1.042
0.35	2.322	0.528	1.068
0.40	2.154	0.543	1.084

Fig. 5. The three symbols in the same figure correspond to the three average profiles and MAHs shown in Fig. 4 and clearly follow the same relation. The dotted line in Fig. 5 shows the best-fit relation of the form

$$c [M(\rho)] = a_1 (1 + a_2 \times c [\text{MAH}])^{a_3}, \quad (6)$$

which is accurate to better than 3% over the range $-0.5 \leq \log c [\text{MAH}] \leq 1.5$. The best-fit parameters are provided in Table 1.

Note that this is consistent with earlier claims that

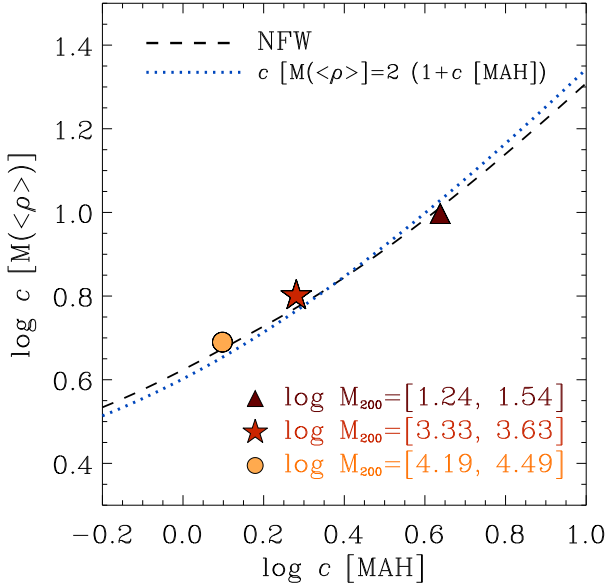


Figure 5. Relation between concentration parameters obtained from NFW fits to the average accretion histories and mass profiles shown in Fig. 4. The dashed curve indicates the expected concentration-concentration dependence given the correlations shown in the middle-right panel of Fig. 3, assuming an NFW profile. The dotted line shows the best fit obtained using Eq. 6; the parameters of the fit are provided in Table 1. Note that the relation is rather shallow, indicating that even halos whose accretion histories differ greatly may have similar concentrations, a result consistent with the weak mass-concentration dependence reported in earlier work.

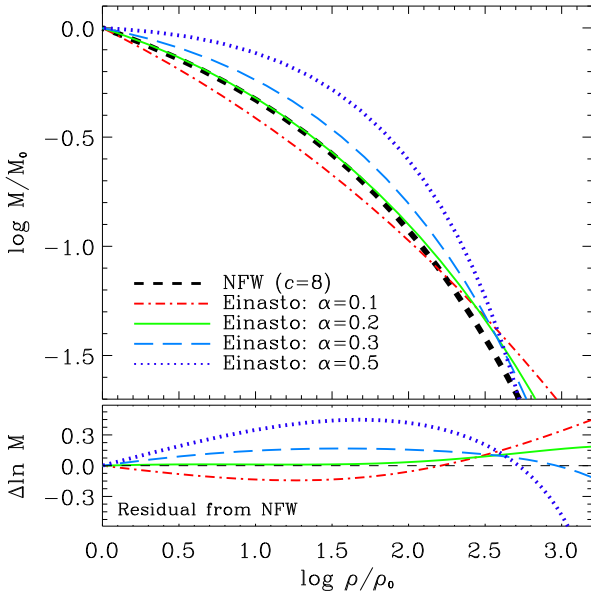


Figure 6. Mass accretion histories, $M(\rho_{\text{crit}})$, corresponding to Einasto profiles, compared with NFW. Note that NFW resembles closely an Einasto profile with $\alpha \sim 0.18$ or so. Larger or smaller values of α correspond to halos that have been assembled more or less rapidly than the NFW curve, respectively. Residuals from NFW are shown in the bottom panel.

halo concentration is linked to the time when halo growth switches from a fast- to a slow-accretion phase (Wechsler et al. 2002; Zhao et al. 2003). In our interpretation, since both the MAH and the mass profile follow the same NFW shape the scale radius of one tracks that of the other: the “curvature” of the MAH is therefore reflected in that of the mass profile. Note as well that the relation shown in Fig. 5 is rather weak; in other words, even large changes in the MAH map onto a small range of concentrations in the mass profiles. This is at the root of the weak correlation between concentration and virial mass reported in earlier work (see, e.g., Neto et al. 2007).

4.4 Einasto accretion histories and mass profiles

The striking similarity between the shapes of the MAH and mass profile discussed above suggests an explanation for why halos that are outliers in the mass-concentration relation tend to have mass profiles that differ more significantly from NFW (i.e., they have α parameters that differ from 0.18, see Fig. 2). In this interpretation, outliers in M_{200} - c have MAH shapes that differ systematically from the mean, NFW-like shape.

In order to test this, we may use the Einasto formula to fit both MAH and mass profiles. Fig. 6 shows Einasto M - ρ profiles for various values of α , and compares them with an NFW profile of the same concentration. (This figure uses the same scalings as Fig. 4.) As stated earlier, over the range of mass and density plotted here the NFW profile is essentially indistinguishable from an $\alpha = 0.18$ Einasto profile, but systematic deviations become apparent for other values of α . Interpreting Fig. 6 as a mass accretion history, we see that $\alpha > 0.18$ corresponds to halos that are assembled more rapidly than expected from the NFW shape. The opposite holds for $\alpha < 0.18$. This behaviour is clearly seen in the residuals from NFW, which are shown in the bottom inset of the figure.

The top panels of Fig. 7 show the average $M(\langle\rho\rangle)$ profiles of halos in three different narrow mass bins chosen to have different values of α . These are halos whose Einasto parameters fall in the boxes drawn in the bottom panel of Fig. 2. The best-fit NFW profile for each mass bin (as in Fig. 4) is indicated by a dashed curve in each panel. Deviations from the NFW curve are shown in the residuals panels. As expected, the residuals have different shapes depending on the value of their shape parameter α .

The bottom panels of Fig. 7 show the corresponding average mass accretion histories and compare them with the mean *predicted* MAHs shown in the bottom panels of Fig. 4. The latter are the NFW MAHs that result from the $\langle\rho_{-2}\rangle$ - $\rho_{\text{crit}}(z_{-2})$ correlation shown in Fig. 3. The residuals from this predicted MAH are clearly similar in shape to those in the top panels: in other words, *halos whose mass profiles deviate from NFW have mass accretion histories that deviate from the NFW shape in a similar way.*

Quantitatively, this implies that the best-fit Einasto parameters of both MAHs and mass profiles must be correlated. Since we expect the correlations to be weak (see, e.g., Fig. 5) we group halos by mass, concentration, and shape parameter (as measured from their mass profiles) before fitting Einasto profiles to their corresponding average mass accretion histories. To prevent possible biases induced by

numerical-resolution effects the grouping is such that we retain only well-resolved halos with similar numbers of particles, $25,000 < N_{200} < 50,000$. Statistical fluctuations are reduced by averaging over groups of at least 25 halos, using a grid in the c - α plane with a mesh of width $\delta \log c = 0.079$ and $\delta \alpha = 0.026$.

The results are shown by the heavy symbols in Fig. 8. The left panel shows that the MAH shape parameter is clearly correlated with the shape parameter of the mass profile. Symbols of different colors are used for halos in each of the three mass bins, which correspond to different MS. Note that they all delineate the same trend, despite the fact that they span a range of roughly four decades in virial mass. Note as well that parameters corresponding to individual halos (shown as grey dots in the figure) correlate less well, and that the scatter is larger for the MS-XXL halos. This is because individual MAHs are often quite complex, especially when major mergers are involved or halos are recently assembled and still unrelaxed (even though they pass the relaxation criteria set out in Sec. 2.2), as is the case for many MS-XXL systems (Ludlow et al. 2012). These MAHs cannot be well approximated by the Einasto shape, thus hindering the interpretation of their fit parameters. We therefore focus the discussion on the parameters fit to the averaged profiles, shown with heavy symbols in Fig. 8.

The relation between shape parameters is quite weak (the 1:1 relation is indicated by the dotted line), implying that large variations in MAH shape map onto a narrower range of mass profile shapes. As a result, even halos that assemble early and over a very short period of time, such as those whose MAH is characterized by $\alpha \sim 0.5$ (see Fig. 6), end up with $\alpha \sim 0.25$ mass profiles that differ only slightly from NFW. This is consistent with earlier findings that halos assembled monolithically and without protracted accretion, such as those formed in hot dark matter universes, are nevertheless well approximated by NFW profiles (e.g., Huss et al. 1999; Wang & White 2009).

It also explains why the NFW profile fits rather well halos formed in hierarchical scenarios other than LCDM. For example, the accretion histories of halos formed in scale-free scenarios characterized by a power-law spectrum of density fluctuations, $P(k) \propto k^n$, depends on n , but rather weakly. For given n , the MAH shapes are also, on average, independent of halo mass. Fitting Einasto profiles to accretion histories taken from Zhao et al. (2009), we find that halos that form from white-noise spectra ($n = 0$) have MAHs well described by $\alpha \sim 0.1$. For $n = -2$, on the other hand, the average MAH shape is roughly $\alpha \sim 0.2$. These different MAHs result in only a subtle change in mass profile (see left panel of Fig. 8), which would have been undetectable at the numerical resolution probed by earlier work. It may, however, be behind the claim by Knollmann et al. (2008) that the inner slope of the density profile varies systematically with the spectral index n .

The right-hand panel of Fig. 8 shows, on the other hand, the correlation between the best-fit Einasto concentration parameters of the MAH and mass profiles, for the same set of halos shown in the left-hand panel of the same figure. This is analogous to Fig. 5, but for Einasto, rather than NFW, concentrations. (The NFW c - c correlation is shown by a dashed line.) Because of the extra parameter, the relation between Einasto concentrations depends on α , and is

indicated by the colored lines in the figure for three values of α . The symbol types in both panels are the same, but are colored by α in the right-hand panel (see color bar inset). Note that, for given α , the c - c relation for MS halos follows closely the expected correlations. As for the NFW profile, the concentration-concentration relation for Einasto profiles can also be approximated by Eq. 6. In Table 1 we provide the best-fit parameters obtained by fitting Eq. 6 to these relations for several different values of α .

As in the left panel, grey dots in the right-hand panel of Fig. 8 correspond to fits to individual halo MAH and mass profiles. These clearly follow the same trend as the averaged profiles but with larger scatter. In particular, complexities in the MAH caused by major mergers result at times in extreme values for the “concentration” measured from accretion histories. These affect in particular large mass halos that have recently been assembled. As discussed by Ludlow et al. (2012), many such halos pass the relaxation criteria but are actually out of equilibrium and in a particular phase of their virialization process. These halos are actually responsible for most of the outlier points in Fig. 8. Although a detailed investigation of the accuracy with which our model can predict the concentrations of *individual* halos from their MAHs is beyond the scope of this paper, we plan to return to this subject in forthcoming work.

We conclude that there is strong evidence for a link between the concentration and shape of the mass profile of halos and their accretion histories. The correlations are well-defined but weak, in the sense that even MAHs whose shapes deviate substantially from the mean lead to halos that depart only subtly from the average, NFW-like mass profile. This is probably due to the virialization process, where non-linear effects lead to a substantial but incomplete erasure of memory of the initial conditions from the equilibrium structure of a halo. The structural similarity of CDM halos thus seems to arise from the mass-independence of MAH shapes aided by the homogenizing effect of halo virialization.

5 SUMMARY AND CONCLUSIONS

We have examined the mass profile and accretion histories of equilibrium cold dark matter halos identified in the Millennium Simulation series. As reported in earlier work, halo mass profiles are well approximated by NFW profiles which, at given virial mass, are characterized by a single parameter, the concentration, $c = r_{200}/r_{-2}$. Although in general deviations from the NFW profile are small, improved fits may be achieved using Einasto profiles characterized, at given virial mass, by the concentration and an extra shape parameter, α .

Our main finding is that these parameters are strongly linked to the accretion history of a halo. The mean density within the scale radius, r_{-2} , is directly proportional to the critical density of the Universe at the time when the main progenitor’s mass equals that within r_{-2} . Scaled to these characteristic values of mass and density the shape of the mass accretion history, expressed as $M(\rho_{\text{crit}}(z))$, is, on average, independent of halo mass. Furthermore, this shape is nearly identical to that of the enclosed mass-mean inner density profile ($M(\langle \rho \rangle)$) of the halo at $z = 0$, which can be well approximated by the NFW profile.

This result suggests that the structural similarity of halos of different mass is related to the fact that their accretion histories are independent of mass. It also clarifies how the accretion history determines the concentration of a halo; since accretion history and mass profile follow the same NFW shape, there is a unique correspondence between the “concentration” parameters of either one, as shown in Fig. 5.

This conclusion is strengthened by the finding that halos whose mass profiles deviate from NFW and are better approximated by Einasto profiles, have mass accretion histories that deviate from the NFW shape in a similar way. This suggests that the extra shape parameter of the Einasto profile arises because some halos have accretion history shapes that differ from NFW. Indeed, fitting Einasto profiles to both $M(\langle\rho\rangle)$ and $M(\rho_{\text{crit}}(z))$ yields correlated concentration and shape parameters. The correlations are clear but weak, implying that only halos whose accretion histories deviate strongly from the NFW shape would have mass profiles that deviate noticeably from the average, NFW-like shape. We ascribe this result to the convergent effects of virialization, which partially erase the memory of initial conditions from the halo structure.

Our results suggest that the density profiles of halos formed in hierarchical scenarios other than CDM or monolithically, as in a hot dark matter Universe, are not truly self-similar. The deviations from similarity, however, are subtle, and a dedicated program of high-resolution numerical simulations is needed in order to validate this prediction.

We may use these findings to predict the dependence of halo concentration on mass and redshift, as well as the influence of varying the spectral index or the cosmological parameters, provided that realistic accretion histories are available, either through direct numerical simulation or through well-tested semi-analytic modeling (e.g., Monaco et al. 2002; van den Bosch 2002; Zhao et al. 2009). Such studies would help to reveal any shortcomings in our interpretation and should shed further light onto the mechanisms responsible for CDM halo structure. We plan to address these issues in a forthcoming paper.

Finally, our findings provide some endorsement to the many previous studies that have sought a link between the final structure of a halo and its evolutionary history (e.g., Bullock et al. 2001; Wechsler et al. 2002; Alvarez et al. 2003; Zhao et al. 2003; Tasitsiomi et al. 2004; Lu et al. 2006; Zhao et al. 2009; Wong & Taylor 2012) but still fall short of providing a full account of what determines the structure of dark matter halos. Hopefully, the link with accretion history we describe here will help to guide future theoretical work in order to unravel the mechanism at the root of the remarkable structural similarity of dark matter halos.

ACKNOWLEDGEMENTS

We would like to thank Gerard Lemson for useful discussions, and the Virgo Consortium for access to the MS data. We would also like to thank the anonymous referee for a prompt report that helped improve our paper. ADL acknowledges financial support from the SFB (956) from the Deutsche Forschungsgemeinschaft. REA is supported by Advanced Grant 246797 GALFORMOD from the European Research Council. MB-K acknowledges support from the

Southern California Center for Galaxy Evolution, a multi-campus research program funded by the University of California Office of Research. VS acknowledges partial support by TR33, ‘The Dark Universe’, of the Deutsche Forschungsgemeinschaft.

This paper has been typeset from a $\text{\TeX}/\text{\LaTeX}$ file prepared by the author.

REFERENCES

- Alvarez M. A., Ahn K., Shapiro P. R., 2003, in Reyes-Ruiz M., Vázquez-Semadeni E., eds, *Revista Mexicana de Astronomía y Astrofísica Conference Series Vol. 18 of Revista Mexicana de Astronomía y Astrofísica*, vol. 27, Density Profiles of Dark Halos from their Mass Accretion Histories. pp 4–7
- Angulo R. E., Springel V., White S. D. M., Jenkins A., Baugh C. M., Frenk C. S., 2012, *MNRAS*, 426, 2046
- Avila-Reese V., Firmani C., Hernández X., 1998, *ApJ*, 505, 37
- Boylan-Kolchin M., Springel V., White S. D. M., Jenkins A., Lemson G., 2009, *MNRAS*, 398, 1150
- Bullock J. S., Kolatt T. S., Sigad Y., Somerville R. S., Kravtsov A. V., Klypin A. A., Primack J. R., Dekel A., 2001, *MNRAS*, 321, 559
- Crone M. M., Evrard A. E., Richstone D. O., 1994, *ApJ*, 434, 402
- Dalal N., Lithwick Y., Kuhlen M., 2010, *ArXiv e-prints*: 1010.2539D
- Davis M., Efstathiou G., Frenk C. S., White S. D. M., 1985, *ApJ*, 292, 371
- Einasto J., 1965, *Trudy Inst. Astroz. Alma-Ata*, 51, 87
- Eke V. R., Navarro J. F., Steinmetz M., 2001, *ApJ*, 554, 114
- Fillmore J. A., Goldreich P., 1984, *ApJ*, 281, 1
- Frenk C. S., White S. D. M., 2012, *Annalen der Physik*, 524, 507
- Gao L., Navarro J. F., Cole S., Frenk C. S., White S. D. M., Springel V., Jenkins A., Neto A. F., 2008, *MNRAS*, 387, 536
- Gunn J. E., Gott III J. R., 1972, *ApJ*, 176, 1
- Hayashi E., White S. D. M., 2008, *MNRAS*, 388, 2
- Hoffman Y., Shaham J., 1985, *ApJ*, 297, 16
- Huss A., Jain B., Steinmetz M., 1999, *ApJ*, 517, 64
- Jing Y. P., 2000, *ApJ*, 535, 30
- Knollmann S. R., Power C., Knebe A., 2008, *MNRAS*, 385, 545
- Lu Y., Mo H. J., Katz N., Weinberg M. D., 2006, *MNRAS*, 368, 1931
- Ludlow A. D., Navarro J. F., Li M., Angulo R. E., Boylan-Kolchin M., Bett P. E., 2012, *MNRAS*, 427, 1322
- Ludlow A. D., Navarro J. F., White S. D. M., Boylan-Kolchin M., Springel V., Jenkins A., Frenk C. S., 2011, *MNRAS*, p. 937
- Macciò A. V., Dutton A. A., van den Bosch F. C., 2008, *MNRAS*, 391, 1940
- Merritt D., Graham A. W., Moore B., Diemand J., Terzić B., 2006, *AJ*, 132, 2685
- Merritt D., Navarro J. F., Ludlow A., Jenkins A., 2005, *ApJL*, 624, L85

- Monaco P., Theuns T., Taffoni G., Governato F., Quinn T., Stadel J., 2002, ApJ, 564, 8
- Navarro J. F., Frenk C. S., White S. D. M., 1995, MNRAS, 275, 720
- Navarro J. F., Frenk C. S., White S. D. M., 1996, ApJ, 462, 563
- Navarro J. F., Frenk C. S., White S. D. M., 1997, ApJ, 490, 493
- Navarro J. F., Hayashi E., Power C., Jenkins A. R., Frenk C. S., White S. D. M., Springel V., Stadel J., Quinn T. R., 2004, MNRAS, 349, 1039
- Navarro J. F., Ludlow A., Springel V., Wang J., Vogelsberger M., White S. D. M., Jenkins A., Frenk C. S., Helmi A., 2010, MNRAS, 402, 21
- Neto A. F., Gao L., Bett P., Cole S., Navarro J. F., Frenk C. S., White S. D. M., Springel V., Jenkins A., 2007, MNRAS, 381, 1450
- Nusser A., Sheth R. K., 1999, MNRAS, 303, 685
- Pontzen A., Governato F., 2013, MNRAS, p. 561
- Power C., Navarro J. F., Jenkins A., Frenk C. S., White S. D. M., Springel V., Stadel J., Quinn T., 2003, MNRAS, 338, 14
- Quinn P. J., Salmon J. K., Zurek W. H., 1986, Nature, 322, 329
- Salvador-Sole E., Solanes J. M., Manrique A., 1998, ApJ, 499, 542
- Springel V., White S. D. M., Jenkins A., Frenk C. S., Yoshida N., Gao L., Navarro J., Thacker R., Croton D., Helly J., Peacock J. A., Cole S., Thomas P., Couchman H., Evrard A., Colberg J., Pearce F., 2005, Nature, 435, 629
- Springel V., White S. D. M., Tormen G., Kauffmann G., 2001, MNRAS, 328, 726
- Stadel J., Potter D., Moore B., Diemand J., Madau P., Zemp M., Kuhlen M., Quilis V., 2009, MNRAS, 398, L21
- Tasitsiomi A., Kravtsov A. V., Gottlöber S., Klypin A. A., 2004, ApJ, 607, 125
- Taylor J. E., Navarro J. F., 2001, ApJ, 563, 483
- van den Bosch F. C., 2002, MNRAS, 331, 98
- Wang J., White S. D. M., 2009, MNRAS, 396, 709
- Wechsler R. H., Bullock J. S., Primack J. R., Kravtsov A. V., Dekel A., 2002, ApJ, 568, 52
- Williams L. L. R., Babul A., Dalcanton J. J., 2004, ApJ, 604, 18
- Wong A. W. C., Taylor J. E., 2012, ApJ, 757, 102
- Zhao D. H., Jing Y. P., Mo H. J., Börner G., 2003, ApJL, 597, L9
- Zhao D. H., Jing Y. P., Mo H. J., Börner G., 2009, ApJ, 707, 354